Optics & Laser Technology 175 (2024) 110753

Contents lists available at ScienceDirect

Optics and Laser Technology

journal homepage: www.elsevier.com/locate/optlastec

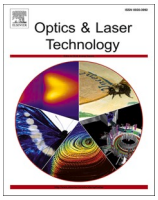

Ultra-high-resolution phase demodulation based miniature fiber-optic accelerometer at low and medium frequencies

Jiayu Huang [a,b], Yajie Zhang [a], Min Guo [c,d,*], Guangyin Zhang [e], Xinyu Zhao [a], Chenxi Li [a], Ke Chen [a,*]

[a] School of Optoelectronic Engineering and Instrumentation Science, Dalian University of Technology, Dalian, Liaoning 116024, China
[b] DUT-BSU Joint Institute, Dalian University of Technology, Dalian, Liaoning 116024, China
[c] Department of Physics, Shaoxing University, Shaoxing 312000, China
[d] Zhejiang Engineering Research Center of MEMS, Shaoxing University, Shaoxing 312000, China
[e] Department of Electrical and Computer Engineering, University of Pittsburgh, Pittsburgh, PA, USA

ARTICLE INFO

Keywords:
Vibration measurement
Fiber-optic accelerometer
Fabry–Perot interferometer
Phase demodulation

ABSTRACT

A miniature fiber-optic Fabry–Perot (F-P) accelerometer based on phase demodulation is demonstrated for improving sensitivity. The accelerometer is composed of a 11.5 mm diameter cylindrical outer frame, a spring-like diaphragm with a loaded mass block and optical fiber. This structure is not only simple and easy to manufacture, but also greatly improves the performances of the accelerometer. The F-P cavity length is demodulated by phase demodulation with abundant advantages of wide dynamic range, high resolution, independent of fiber loss and light intensity fluctuations. The inertial mass displacement indicating a variation in the F-P cavity length is demodulated and converted to acceleration. Through experimental verification, the resonant frequency of the accelerometer is 232 Hz, and axial sensitivity is flat in 30–180 Hz. The average sensitivity of the flat area is 17.55 μm/g and the transverse crosstalk is around 3 %. The resolution of the sensing system is 2.8 μg within a ±3 mm maximum measurement range by experimental tests. This work gives a fitting option to monitor low and medium frequency vibration in a large range of areas.

1. Introduction

Compared with conventional electric sensors, fiber-optic sensors have attracted great deal of attentions due to their unique advantages of high sensitivity, anti-electromagnetic interference and remote detection [1–4]. One of the crucial applications of fiber-optic sensors is fiber-optic accelerometers (FOAs). Currently, FOAs have been applied in structural health monitor [5], aerospace industry [6,7], railway health monitoring [8,9] and seismic monitoring [10].

There are abundant various technologies to develop FOAs. Fiber Bragg gratings (FBGs) is an important application of these technologies to develop FOAs [11]. By the detection of dynamic wavelength shift with induced vibration, the deformation of the sensor caused by the applied acceleration can be measured. For FBG accelerometers, there are different types of FBGs such as Chirped FBG (CFBG) [12], Tilted FBGs (TFBGs) [13], Phase-shifted Bragg grating (PSBG) [14] and so on. It is possible to optimize resolution, low and medium frequency response by using them. Various mechanical structures can also improve their sensitivity by optimizing the vibration-strain conversion efficiency [15]. Some typical FBG accelerometers were designed such as a hinge-shaped sensitization structure within a working frequency range (30–300 Hz) and corresponding sensitivity (57.7 pm/g) [16], a V-double mass block within a wide working frequency (20–340 Hz) and an optimal sensitivity (66.84 pm/g) [17], a cantilever accelerometer within flat region (20–220 Hz) and a larger sensitivity (149.8 pm/g) [18]. For sensitivity optimization, an accelerometer with a short bonding gap could obtain sensitivity of 1771 pm/g [19]. Besides, a dual short FBG accelerometer based on flexible hinge was proposed with an optimal sensitivity (2167.1 pm/g) at a low frequency range (10–50 Hz) [20]. However, the sensitivity, resolution and dynamic range of them are usually limited by the optical fiber stiffness and the spectral range of the FBG operation [21–23].

Fiber-optic accelerometers is developed by Fiber-optic Fabry-Perot (F-P) interferometer. Compared to FBG sensors, fiber-optic F-P accelerometers have higher sensitivity, large working frequency range and resolution [24–26]. Applied acceleration or sound pressure can cause

* Corresponding authors.
E-mail address: chenke@dlut.edu.cn (K. Chen).

https://doi.org/10.1016/j.optlastec.2024.110753
Received 17 November 2023; Received in revised form 20 January 2024; Accepted 23 January 2024
Available online 29 February 2024

the sensor to change its cavity length to measure the applied value. By detecting the changes in F-P cavity length, the acceleration or sound pressure can be obtained. For the measurements of cavity length, light-intensity demodulation, phase demodulation and optical cross-correlation demodulation are usually raised. Light-intensity demodulation measures dynamic physical quantities based on the relationship between the detected light power and the cavity length [27,28]. Wei et al. designed a F-P acoustic detector by 3D printing technology. With ingenious structural design, a low minimum detectable pressure level (4.71 mPa/ Hz1/2@100 kHz) and high bandwidth (366.05 kHz-467.84 kHz) were obtained [29]. Wang et al. produced a fiber-optic F-P accelerometer within a higher resolution (982 ng) and a thin dynamic range (10–90 Hz) [30]. Zhao et al. reported a mesh diaphragm with special structure (mass-loaded structure) which achieves a high sensitivity (3.86μ m/g) within a fitting dynamic range (10–120 Hz) [31]. Intensity demodulation methods control the static working point at the orthogonal phase point of the interfering signal, i.e., the Q point. The measured cavity length varies over λ/8 length range centered on the Q point and detected range is only λ/4. Therefore, even if the Q-point is set at the beginning, the parameter will drift over time because of temperature fluctuations and external environmental disturbances reduced the accuracy of demodulation of the F-P cavity length. At the same time, demodulation dynamic range will be confined and distortion of measured signal may also occur. The optical cross-correlation demodulation method was originally developed by adjusting the cavity length of the reference F-P cavity to match the sensing F-P cavity [32]. When their F-P cavity lengths are adjusted to be identical, the optical correlation interference spectrum will be maximized, and the F-P cavity length is thus measured [33,34]. The cross-correlation demodulation has ample advantages including structural simplicity and high stability. However, cavity length of both F-P cavity of the cross-correlation must be accurately matched which is very hard. For phase demodulation, it is a demodulation method of cavity length by extracting phase information of the measured interference spectrum. Therefore, it has received much attention due to wide dynamic range, high resolution, and independence from fluctuations in light source power and fiber loss. Li et al. conducted researches on fiber optic accelerometer based on phase demodulation with a sensitivity of 3.8 nm/g and a resolution of 263 ng [35]. To simplify the calculation process, Yu et al. presented Buneman frequency estimation and used it for phase demodulation [36]. A high-performance computer is required to perform this method, so this algorithm was optimized and used to demodulate cantilever microphone by Chen et al. [37–40].

In this paper, a miniature ultrahigh-resolution and ultrahigh-sensitivity fiber-optic F-P accelerometer is presented. The F-P accelerometer was made of a housing with a diameter of 11.5 mm and a spring-like diaphragm made of stainless steel, which was optimized by finite element analysis. At the same time, we report an ultra-high-resolution F-P phase demodulation method white light interferometry (WLI) demodulation method. The WLI demodulation scheme can achieve high stability, high-speed measurement. Combining them and constructing a fiber-optic sensing system, the performances of the system were evaluated in lab tests.

2. Principle and simulation analysis

The F-P fiber-optic accelerometer (FOA) is comprised of optical fiber, ceramic ferrule, stainless steel diaphragm, stainless steel mass block and protective shell (Fig. 1(a)). The ceramic ferrule and fiber are fixed on the shell by a hole. The surface of the fiber and the diaphragm are used as the reflector and their tips form the F-P cavity. The block mass is attached on the center of the diaphragm with spring-like structure (Fig. 1 (b)) and the physical photograph of the sensor is displayed in Fig. 1 (c). The original cavity length is 0.4 mm to improved visibility and contrast of interference fringes. Table 1 lists other detailed parameters of the FOA.

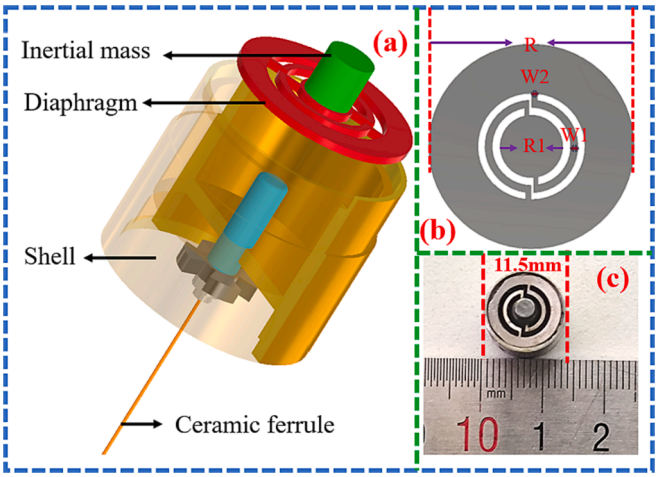

Fig. 1. (a) Structure diagram of the spring-like diagram based fiber-optic F-P accelerometer. (b) Cross-section of the stainless steel diaphragm. (c) Physical image of the sensor element.

Table 1
Parameters of the FOA.

Symbol	Value	Description
T	0.1 mm	Thickness of diaphragm
T_1	3 mm	Thickness of inertial mass
E_1	190000 MPa	Young's modulus of the shell and diaphragm
ρ	8000 kg/m^3	Density of the shell and diaphragm
ν	0.31	Poisson's ration of the stainless steel
R	11.5 mm	Diameter of diaphragm
R_1	3 mm	Diameter of inertial mass
M_{eff}	0.17 g	Total mass of the inertial mass
g	9.81 m/s^2	Acceleration of gravity
W_1	0.4 mm	Beam width
W_2	0.3 mm	Connection width

Supposing that axis acceleration is applied to the FOA, the acceleration of entire accelerometer is a_{in}. If the signal is a sine or cosine function, then the amplitude-frequency characteristic $A(f)$ and K_{eff} of the accelerometer can be obtained as follows [41]:

$$A(f) = \frac{1}{\sqrt{\left[1-\left(\frac{f}{f_0}\right)^2\right]^2 + (2c\frac{f}{f_0})^2}} \tag{1}$$

$$K_{eff} = \frac{Q\pi ET^3}{3R^2(1-\nu)^2\left(\frac{b^2-1}{4b^2} - \frac{ln^2 b}{b^2-1}\right)} \tag{2}$$

where E_1 is the elastic modulus of the stainless steel, ν is Poisson's ratio of the stainless steel, T is the diaphragm thickness, R is the radius of the diaphragm, b is the mass-load solidity ratio($b = R/R_1$) and R_1 is the inertial mass radius, Q is the reduction in stiffness due to the mesh structure. f is the frequency of applied vibration, f_0 describes the resonant frequency of the accelerometer defined as [42]:

$$f_0 = \frac{1}{2\pi}\sqrt{\frac{K_{eff}}{M_{eff}}} \tag{3}$$

where M_{eff} is effective mass of the sensing system.

The mass of the cylindrical block is much larger than the elastic diaphragm. Therefore, the equivalent mass of the overall elastic structure can be approximated as the mass block. When the parameters of the FOA is determined, the displacement is proportional to the applied acceleration a_{in}. According to Hooke's Law, the on-axial acceleration a_{in}

can be calculated as [31]:

$$a_{in} = \frac{Q\pi ET^3\Delta y}{3M_{eff}R^2(1-\nu)^2\left(\frac{b^2-1}{4b^2}-\frac{ln^2 b}{b^2-1}\right)} \tag{4}$$

Furthermore, the sensitivity S_0 can be expressed as:

$$S_0 = \frac{\Delta y}{a_{in}} = \frac{3M_{eff}R^2(1-\nu)^2\left(\frac{b^2-1}{4b^2}-\frac{ln^2 b}{b^2-1}\right)}{Q\pi ET^3} \tag{5}$$

For the dynamic FOA, sensitivity will be impacted by frequency characteristic which can be expressed as:

$$S_D = S_0 A(f) \tag{6}$$

To correspond to the theoretical accounts, the finite element analysis software COMSOL was used to perform the simulation. According to Eq. (6), the acceleration a_{in} is proportional to the variation of F-P cavity length Δy. Considering M_{eff}, E, Q, T, b and ν are constants and then importing these parameters of the sensing system as Table 1 into COMSOL. With axial acceleration of 1 g applied on the FOA, the central deformation distribution can be observed to be 18.26 μm (Fig. 2). With change in frequency and constant acceleration, the ratio of cavity length to acceleration cavity length called frequency response at different frequencies will be obtained (Fig. 3). Based on the Fig. 3, it can be known that the resonant frequency of the accelerometer is 235 Hz.

From the above results, the cavity length must be demodulated to evaluate performances of sensing system. Therefore, white light interferometry (WLI) demodulation is used to obtain cavity length. When a beam of light is incident on the FOA, it will be reflected and refracted many times between the end face of the optical fiber and the inner surface of the diaphragm. The multi-beam interference effect will be generated between the reflected beams. The reflectivity of the F-P interferometry surface is approximately 4 %, so this process of light propagation can be equated to a two-beam interference. Therefore, the reflected light intensity I_R for two-beam interference is expressed as [43]:

$$I_R = 2I_0\left[1+\gamma cos\left(\frac{4\pi(y+\Delta y)}{\lambda}+\pi\right)\right] \tag{7}$$

where I_0 is the intensity of broadband light, γ is the fringe visibility, y is the original cavity length, Δy is the variation of the cavity length, and λ is the central wavelength of the broadband light.

Before performing a WLI demodulation of the cavity length, the interference spectrum of the reflected light must be obtained. Besides,

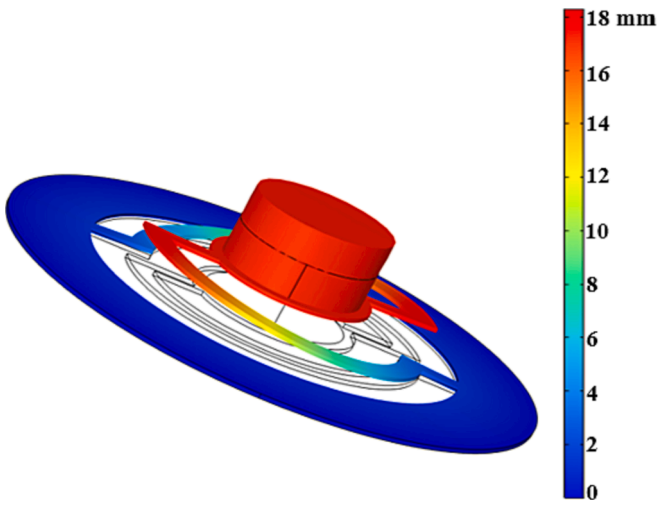

Fig. 2. Simulated total deformation distribution with acceleration of 1 g.

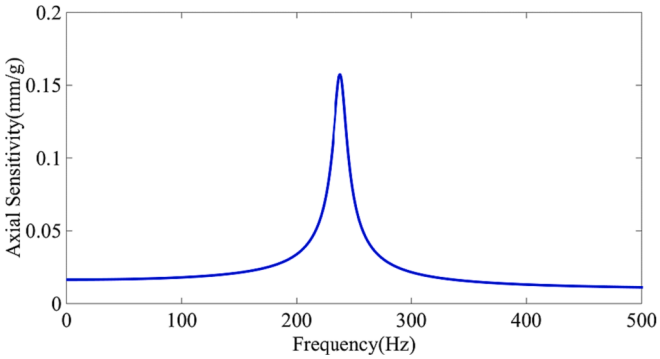

Fig. 3. Simulated frequency response of the accelerometer.

the parameters determined by Zemax, including the F-P cavity length y, can optimize the interference spectrum and intensity contrast. The simulated F-P interference fringe (Fig. 4 (a)) and the acquired actual F-P interference intensity distribution (Fig. 4 (b)) are under the optimal cavity length 0.4 mm. After determining the parameters of the FOA and acquiring the spectral signal, extracting the phase information of the interference spectrum can obtain cavity length information. When axial acceleration is applied to the FOA, the variation in F-P cavity length can be acquired by WLI demodulation algorithm and it's nearly proportional to the acceleration. Then the acceleration signal value can be calculated according to a specific mathematical relationship.

3. Sensing and demodulation system design

The diagram of the sensing system (Fig. 5 (b)) and the internal photograph of the F-P sensing instrument (Fig. 5 (b)) are displayed to clearly state their roles. In the sensing instrument, a super luminescent diode (SLD) was used to excite broadband light with a common wavelength 1550 nm and a full width at half maximum (FWHM) of 45 nm. The F-P interference signal formed by the broadband light passing through the fiber-optic accelerometer (FOA) is collected by a spectral module (I-MON-256-OEM, Ibsen) with highest vibration signal rate of 10 kHz which is consisted of a collimating lens, two transmission gratings, a focusing concave lens and an image detector. Acquired spectral signal was received and transferred to Field Programmable Gate Array (FPGA) circuit by a 256-pixel image detector. The FPGA circuit is composed of a FPGA chip, an analogue-to-digital converter (ADC) chip, a DAC chip and an RS232 communication interface which can accomplish high-speed acquisition and real-time processing of the F-P interference spectrum [44–46]. Spectrum normalization, FFT, interpolation and Buneman frequency estimation are integrated in the FPGA circuit. Among them, Buneman frequency estimation is used for peak evaluation to obtain the change in cavity length by phase demodulation [47]. Buneman frequency estimation reduces the amount of computation and accurately finds the location of the maximum value. The advantages of this method are very simple and the computational effort is very small. Moreover, it is more accurate and has a higher resolution for purely single frequency signals with fractional frequencies. After signal processing, acquired signal is filtered and transferred to computer to demodulate cavity length.

The probe light propagates through the circulator to the FOA. Afterward, optical signals were converted into electrical signals and demodulated by white light interferometry (WLI) demodulation algorithm. The FOA and a commercial piezoelectric accelerometer (PEA) with a sensitivity of 50 mV/g were fixed on a vibration table. The vibration table can produce signals of sinusoidal acceleration within adjustable frequency and amplitude. When it generated vibrating wave, the commercialized PEA would output voltage signal obtained by a data acquisition card (DAQ) and then the voltage signal would be translated into acceleration signal as a reference.

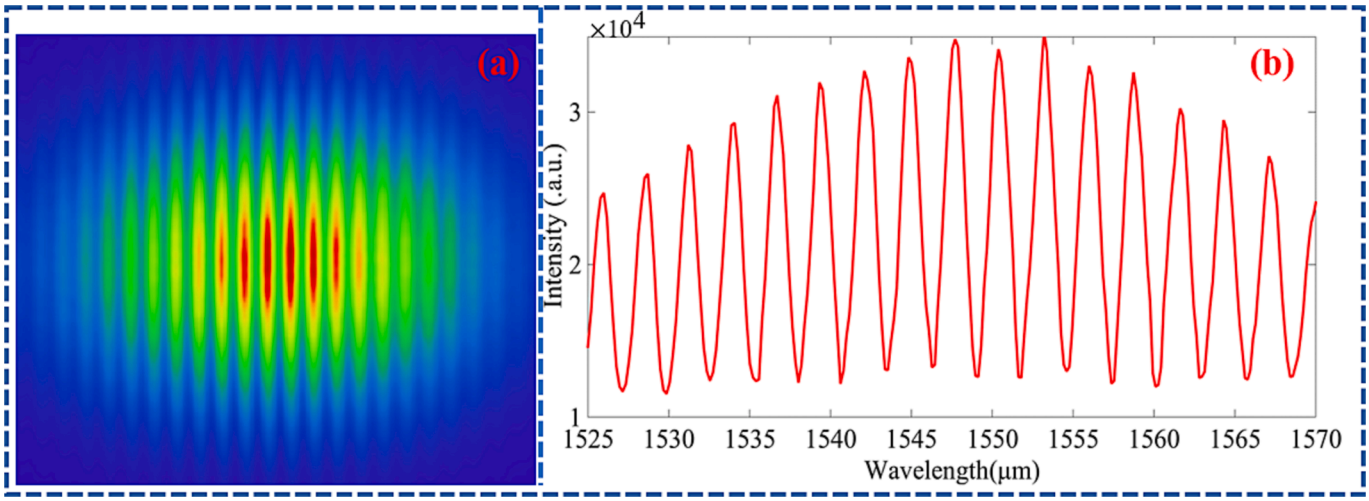

Fig. 4. (a) Simulated F-P spot size by Zemax simulation. (b) Acquired actual F-P interference spectrum.

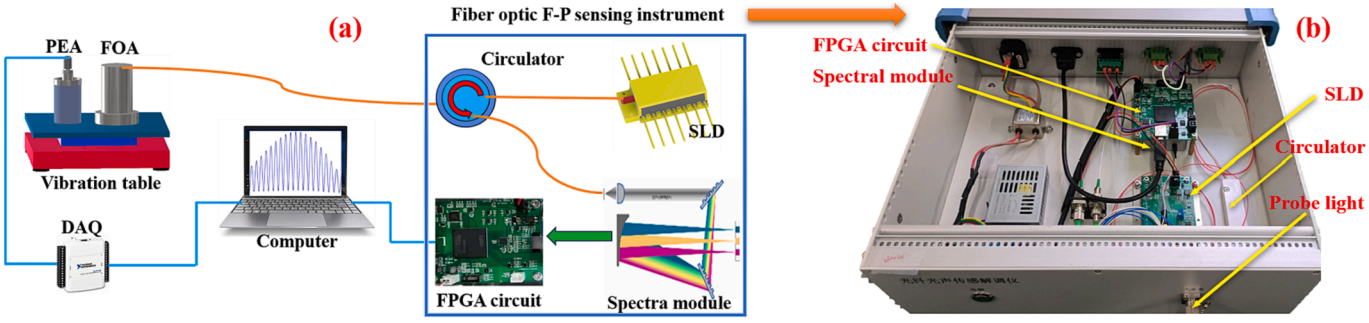

Fig. 5. (a) Diagram of the sensing system for vibration/acoustic measurement. (b) Internal photograph of F-P sensing instrument.

4. Experiments and results analysis

4.1. Measurement of frequency response and axial sensitivity

To test frequency response and axial sensitivity of the accelerometer, an excitation signal with an increase in frequency from 20 Hz to 350 Hz was applied by the vibration table. The piezoelectric accelerometer (PEA) used as a reference with a sensitivity of 50 mV/g and fiber-optic accelerometer (FOA) were fixed on the vibration table. The cavity length changes of FOA and the acceleration changes of PEA could be measured at a same frequency.

The frequency response curve was shown through calculating and data processing (Fig. 6 (a)). The resonant frequency of the accelerometer is 232 Hz, which is similar with the simulation of 235 Hz. In addition, the average sensitivity is 17.55 μm/g with a range of frequency from 30 Hz to 180 Hz which is also close to the simulation of 18.26 μm/g and the deviation of the sensitivities do not exceed 3 dB. The average sensitivity of transverse crosstalk direction is 0.446 μm/g which is approximately 3 % of the axial direction (Fig. 6 (b)), and it is much less than axial direction.

To further evaluate the performances of the sensing system, the stability and linearity in flat frequency range were separately measured. Three selected frequencies of 40, 80 and 120 Hz were applied to the FOA and PEA by vibration table, the time-domain spectrums of cavity length changes and acceleration changes were measured and shown (Fig. 7). They have stable trigonometric waveforms, the sensitivity at each of the three frequencies can be calculated as 17.63 μm/g, 17.75 μm/g and 17.28 μm/g. The linear relationship between the acceleration values and the cavity length values were also acquired with the change of excitation acceleration (Fig. 8). The linear fit coefficients are 0.9992, 0.9942 and

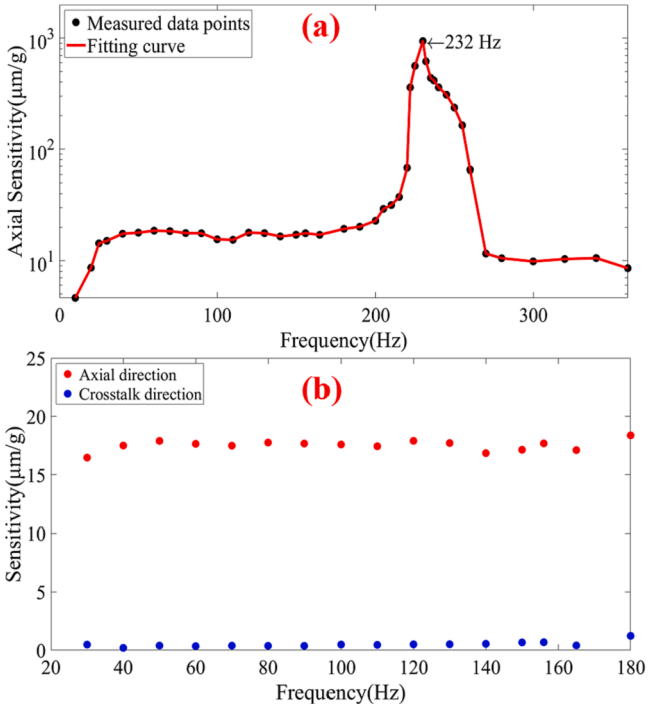

Fig. 6. (a) Measured axial sensitivity. (b) Comparison of sensitivity in both directions.

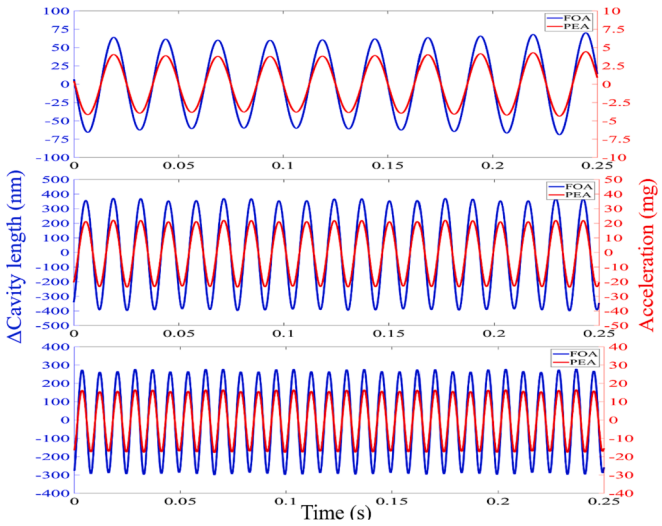

Fig. 7. Measured time domain of cavity length changes by FOA and acceleration changes by PEA when frequencies are 40 Hz, 80 Hz and 120 Hz.

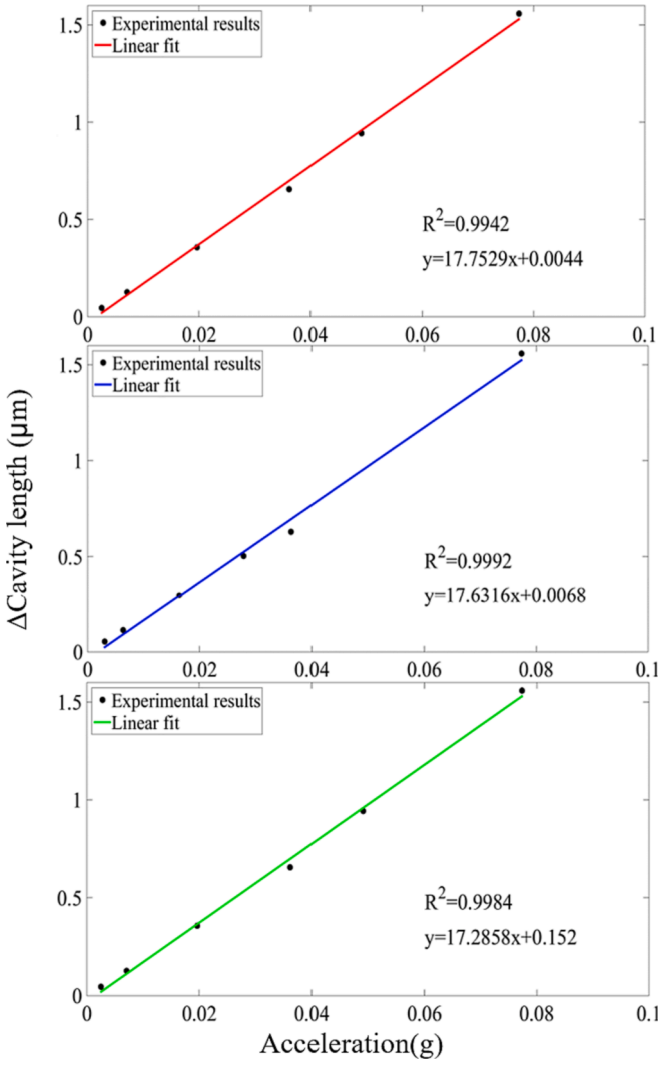

Fig. 8. Measured linearity when the frequencies from top to bottom are 40 Hz, 80 Hz and 120 Hz.

0.9984, respectively. Therefore, the sensing system has excellent stability and linearity in the working range.

4.2. Measurement range and acceleration resolution

The axial displacement given by the vibration table was first gradually increased and then gradually decreased by control panel (Fig. 9). There are three times ascending and descending and the maximum measurement range can be observed as −3 μm to 3 μm without distortion and saturation. This approach is more reasonable than to create a large vibration caused by directly striking the sensor. If the sensor is tapped directly, the sensor may cause formation or even damage, and the detected waveform will be easily deformed. Therefore, the maximum measurable acceleration can be calculated as −174 mg to 174 mg.

To evaluate the long-term noise level and assess the minimum detection acceleration of the system, the accelerometer was placed in a soundproof box. The noise level was measured over 1000 s and the standard deviation (1σ) is 50 pm (Fig. 10 (a)). According to the sensitivity 17.55 μm/g, the resolution can be calculated as 2.8 μg. Allan-Werle deviation was also used to evaluate the performance of the accelerometer [48]. When the average time is 100 s, the detection limit of acceleration reaches 28 ng (Fig. 10 (a)). In addition, a comparison between our work and other reported work is displayed in Table 2. The results show that the sensing system has excellent performance compared to some of the current work.

5. Conclusion

In conclusion, a miniature fiber-optic Fabry-Perot accelerometer is proposed to achieve ultra-high resolution and sensitivity vibration detection at low-frequency and medium-frequency. Finite element analysis is used to simulate the axial sensitivity and the performance of accelerometer. The WLI demodulation based on phase demodulation is used to demodulate the cavity length, and the sensitivity and resolution of the accelerometer are obtained after that. The vibration detection and digital locking equalization functions are integrated by the FPGA circuit, increasing the speed and stability of the system. With a well-designed sensing system and a good agreement with simulation results, the resonance frequency was 232 Hz, and the axial sensitivity of the accelerometer was measured to be 17.55 μm/g in the 30–180 Hz. Furthermore, the transverse crosstalk is approximately 3 %. The acceleration resolution was calculated to be 2.8 μg and maximum cavity length was measured to be ±3 μm. With unique capability of the optic-fiber Fabry–Perot accelerometer, this new technology is promising for aerospace, low- and medium-frequency vibration signals and mechanical equipment.

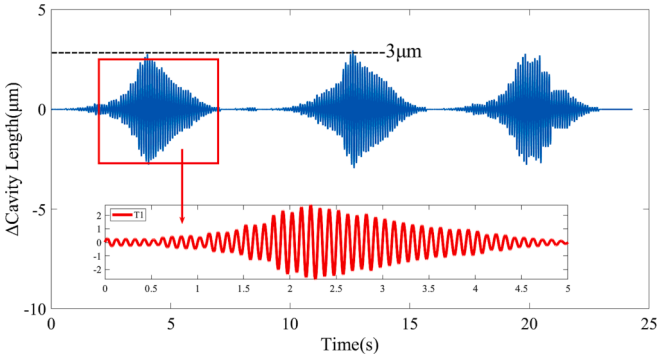

Fig. 9. Measured maximum measurement range of cavity length with three times gradual rises and falls of vibration.

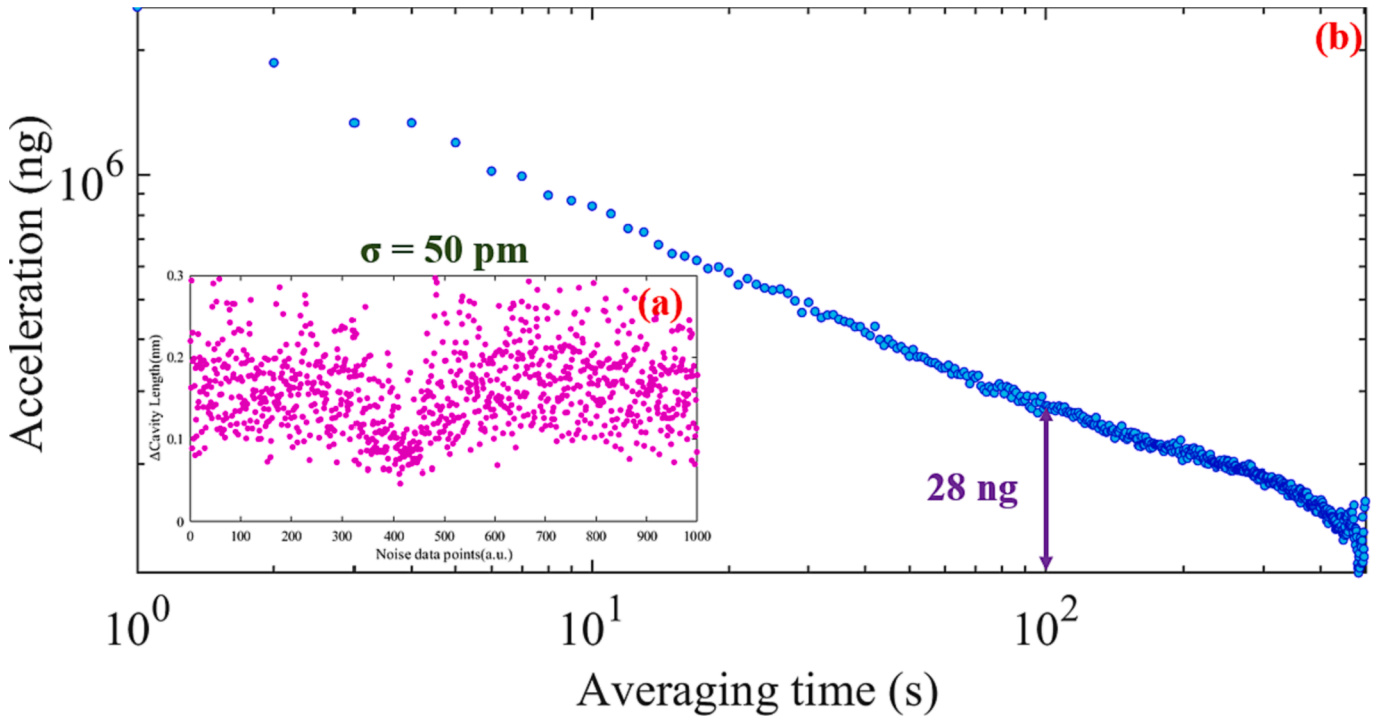

Fig. 10. (a) Detected noise points in a soundproof box. (b) Allan deviation of the noise signal.

Table 2
Comparison between our work and other reported schemes.

Authors	Sensing method	Resonance frequency	Bandwidth	Resolution	Sensitivity
Shao et al. [17]	FBG	860 Hz	20–340 Hz	–	66.95 pm/g
Li et al. [19]	FBG	150 Hz	10–100 Hz	–	1.711n m/g
Chen et al. [20]	FBG	63 Hz	10–50 Hz	–	2.167 nm/g
Li et al. [35]	FPI	800 Hz	30–300 Hz	263 μg	3.81 nm/g
Zhao et al. [31]	FPI	270 Hz	10–120 Hz	8.5 μg	3860n m/g
This work.	FPI	232 Hz	30–180 Hz	2.8 μg	17220n m/g

CRediT authorship contribution statement

Jiayu Huang: Writing – review & editing, Writing – original draft, Resources, Investigation. **Yajie Zhang:** Supervision, Formal analysis. **Min Guo:** Validation, Formal analysis, Data curation. **Guangyin Zhang:** Supervision, Software. **Xinyu Zhao:** Visualization, Validation. **Chenxi Li:** Validation, Formal analysis. **Ke Chen:** Software, Funding acquisition, Formal analysis, Conceptualization.

Declaration of competing interest

The authors declare that they have no known competing financial interests or personal relationships that could have appeared to influence the work reported in this paper.

Data availability

No data was used for the research described in the article.

Acknowledgements

The authors would like to acknowledge the financial supports from the National Nature Science Foundation of China (62275040, 61905034), Dalian High-level Talent Innovation Support Plan (2019RQ010).

References

[1] M.-Q. Chen, T.-Y. He, Y. Zhao, Review of femtosecond laser machining technologies for optical fiber microstructures fabrication, Opt. Laser Technol. 147 (2022) 107628.
[2] Y. Guo, D. Zhang, Z. Zhou, L. Xiong, X. Deng, Welding-packaged accelerometer based on metal-coated FBG, Chin. Opt. Lett. 11 (7) (2013) 070604.
[3] A. Sabato, C. Niezrecki, G. Fortino, Wireless MEMS-based accelerometer sensor boards for structural vibration monitoring: a review, IEEE Sens. J. 17 (2) (2016) 226–235.
[4] A. Leal-Junior, A. Theodosiou, C. Díaz, et al., Fiber bragg gratings in CYTOP fibers embedded in a 3D-printed flexible support for assessment of human–robot interaction forces, Materials 11 (11) (2018) 2305.
[5] A.P.F. da Costa, H.F.T. Lima, N.J. Alberto, et al., Optical fiber accelerometer system for structural dynamic monitoring, IEEE Sens. J. 9 (11) (2009) 1347–1354.
[6] G. Yan, T. Wang, L. Zhu, F. Meng, W. Zhuang, A novel strain-decoupled sensitized FBG temperature sensor and applications to aircraft thermal management, Opt. Laser Technol. 140 (2021) 106597.
[7] J. Wen, H. Yao, Z.e. Ji, W.u. Bin, X.u. Feng, Self-validating high-g accelerometers through data-driven methods, Sens. Actuators, A 328 (2021) 112803.
[8] K. Yüksel, D. Kinet, V. Moeyaert, et al., Railway monitoring system using optical fiber grating accelerometers, Smart Mater. Struct. 27 (10) (2018) 105033.
[9] W. Huang, W. Zhang, Y. Du, et al., Detection of rail corrugation based on fiber laser accelerometers, Meas. Sci. Technol. 24 (9) (2013) 094014.
[10] G. Gagliardi, M. Salza, P. Ferraro, et al., Design and test of a laser-based optical-fiber bragg-grating accelerometer for seismic applications, Meas. Sci. Technol. 19 (8) (2018) 085306.
[11] T.A. Berkoff, A.D. Kersey, Experimental demonstration of a fiber bragg grating accelerometer, IEEE Photon. Technol. Lett. 8 (12) (1996) 1677–1679.
[12] S. Korganbayev, Y. Orazayev, S. Sovetov, et al., Detection of thermal gradients through fiber-optic chirped fiber bragg grating (CFBG): medical thermal ablation scenario, Opt. Fiber Technol. 41 (2018) 48–55.
[13] H.Y. Wen, Y.C. Hsu, S.Y. Chen, et al., The manufacturing process and spectral features of tilted fiber bragg gratings, Opt. Laser Technol. 134 (2021) 106615.
[14] L. Macedo, E. Pedruzzi, L. Avellar, et al., High-resolution sensors for mass deposition and low-frequency vibration based on phase-shifted bragg gratings, IEEE Sens. J. 23 (3) (2022) 2228–2235.
[15] R. Wang, Y. Li, X. Qiao, Recent advances in multidimensional fiber bragg grating accelerometers, J. Lightwave Technol. (2023).

[16] H.D. Le, C. Chiang, C.N. Nguyen, et al., A novel short fiber bragg grating accelerometer based on a V-type dual mass block structure for low-and medium-frequency vibration measurements, Opt. Laser Technol. 161 (2023) 109131.
[17] M. Shao, J. Liang, H. Gao, D. Yu, X. Qiao, Medium and low frequency fiber bragg grating acceleration sensor based on single-sided single-arc hinge, Opt. Fiber Technol. 69 (2022) 102814.
[18] S. Dang, D. Yu, W. Fan, Cantilever vibration sensor based on fiber bragg grating temperature compensation, Opt. Fiber Technol. 75 (2023) 103183.
[19] Y. Li, Q. Ma, F. Chen, R. Wang, X. Qiao, A flexible hinge accelerometer based on dual short fiber bragg grating, Sensors Actuators a: Physical 344 (2022) 113695.
[20] F. Chen, X. Li, R. Wang, et al., Sensitivity enhancement of fiber-optic accelerometers using thin-cladding fiber bragg gratings, J. Lightwave Technol. 39 (18) (2021) 5988–5994.
[21] Y. Weng, X. Qiao, T. Guo, et al., A robust and compact fiber bragg grating vibration sensor for seismic measurement, IEEE Sens. J. 12 (4) (2011) 800–804.
[22] Q.P. Liu, X.G. Qiao, Zhao, et al., Novel fiber bragg grating accelerometer based on diaphragm, IEEE Sens. J. 12 (10) (2012) 3000–3004.
[23] M.D. Todd, G.A. Johnson, B.A. Althouse, et al., Flexural beam-based fiber bragg grating accelerometers, IEEE Photon. Technol. Lett. 10 (11) (1998) 1605–1607.
[24] Y. Yang, Y. Wang, K. Chen, Wideband fiber-optic fabry-perot acoustic sensing scheme using high-speed absolute cavity length demodulation, Opt. Express 29 (5) (2021) 6768–6779.
[25] C. Ke, Y. Yang, B.o. Zhang, et al., Simultaneous measurement of acoustic pressure and temperature using a fabry-perot interferometric fiber-optic cantilever sensor, Opt. Express 28 (10) (2020) 15050–15061.
[26] K.e. Chen, Z. Gong, M. Guo, et al., Fiber-optic fabry-perot interferometer based high sensitive cantilever microphone, Sens. Actuators, A 279 (2018) 107–112.
[27] X. Mao, S. Yuan, P. Zheng, et al., Stabilized fiber-optic fabry-perot acoustic sensor based on improved wavelength tuning technique, J. Lightwave Technol. 35 (11) (2017) 2311–2314.
[28] Q. Liu, Z. Jing, Y. Liu, et al., Quadrature phase-stabilized three-wavelength interrogation of a fiber-optic fabry-perot acoustic sensor, Opt. Lett. 44 (22) (2019) 5402–5405.
[29] H. Wei, Z. Wu, Y. Wei, et al., 3D Printed Fabry-Perot Acoustic Probe with a Glass Horn Tube 168 (2024) 109977.
[30] Y. Wang, L. Jiang, W. Liu, et al., An in-fiber acceleration sensor based on fabry-perot cavity, in: 2019 18th International Conference on Optical Communications and Networks (ICOCN), 2019, pp. 1–3.
[31] Z. Zhao, Z. Yu, K. Chen, et al., A fiber-optic fabry-perot accelerometer based on high-speed white light interferometry demodulation, J. Lightwave Technol. 36 (9) (2017) 1562–1567.
[32] K. Chen, Z. Wang, M. Guo, et al., Single-mode fiber-optic fabry-perot interferometry sensor based on optical cross-correlation demodulation, Opt. Eng. 58 (2) (2019) 026106.
[33] G. Zhang, Z. Xiong, M. Guo, et al., Low-frequency optical fiber fabry-perot acoustic sensor based on all-phase cross-correlation demodulation, J. Lightwave Technol. 40 (22) (2022) 7431–7438.
[34] M. Guo, K. Chen, G. Zhang, et al., High-sensitivity fiber-optic low-frequency acoustic detector based on cross-correlation demodulation, J. Lightwave Technol. 40 (13) (2022) 4481–4488.
[35] Y. Li, Y. Wang, X. Li, et al., Enhancing the performance of FBG accelerometers by using in-fiber fabry perot interferometers, IEEE Sens. J. 22 (24) (2022) 23931–23936.
[36] Z. Yu, A. Wang, Fast white light interferometry demodulation algorithm for low-finesse fabry-pérot sensors, IEEE Photon. Technol. Lett. 27 (8) (2015) 817–820.
[37] K. Chen, Z. Yu, Q. Yu, Fast demodulated white-light interferometry-based fiber-optic fabry-perot cantilever microphone, Opt. Lett. 43 (14) (2018) 3417–3420.
[38] X. Zhao, H. Qi, Z. Wang, et al., Cantilever enhanced fiber-optic photoacoustic microprobe for diffusion detection of sulfur dioxide, Chemical Sensors and Actuators B (2024) 135340.
[39] X. Zhao, Z. Wang, C. Li, et al., Ultrahigh sensitive trace gas sensing system with dual fiber-optic cantilever multiplexing-based differential photoacoustic detection, Anal. Chem. (2024).
[40] C. Li, M. Guo, Z. Wang, et al., Fiber-optic photoacoustic gas sensor with multiplexed fabry-pérot interferometric cantilevers, Anal. Chem. (2023).
[41] A.S. Gerges, T.P. Newson, J.D.C. Jones, et al., High-sensitivity fiber-optic accelerometer, Opt. Lett. 14 (4) (1989) 251–253.
[42] D.A. Brown, S.L. Garrett, Interferometric fiber optic accelerometer. fiber optic and laser sensors VIII, SPIE (1991, 1367,) 282–288.
[43] Q. Yu, X. Zhou, Pressure sensor based on the fiber-optic extrinsic fabry-perot interferometer, Photonic Sensors 1 (2011) 72–83.
[44] Li C, Qi H, Han X, et al. Ultra-high-speed phase demodulation of Fabry-Perot sensor based on fiber array parallel spectral detection, (2024).
[45] C. Li, X. Zhao, H. Qi, et al., Integrated fiber-optic fabry-perot vibration/acoustic sensing system based on high-speed phase demodulation, Opt. Laser Technol. 169 (2024) 110131.
[46] X. Zhao, C. Li, H. Qi, et al., Integrated near-infrared fiber-optic photoacoustic sensing demodulator for ultra-high sensitivity gas detection, Photoacoustics (2023) 100560.
[47] C. Li, X. Han, F. Ma, et al., Multiplexed fiber-optic photoacoustic sensors for simultaneous detection of multi-point gases, Sens. Actuators B 399 (2024) 134801.
[48] C. Li, Z. Sun, L. Zhou, et al., Microseismic observation enabled by high-sensitivity micromechanical interferometers, IEEE Trans. Ind. Electron. (2023).